3-D moveout inversion in azimuthally anisotropic media with lateral velocity variation: Theory and a case study

Vladimir Grechka* and Ilya Tsvankin*

ABSTRACT

Reflection moveout recorded over an azimuthally anisotropic medium (e.g., caused by vertical or dipping fractures) varies with the azimuth of the source-receiver line. Normal-moveout (NMO) velocity, responsible for the reflection traveltimes on conventional-length spreads, forms an *elliptical* curve in the horizontal plane. While this result remains valid in the presence of arbitrary anisotropy and heterogeneity, the inversion of the NMO ellipse for the medium parameters has been discussed so far only for horizontally homogeneous models above a horizontal or dipping reflector.

Here, we develop an analytic moveout correction for weak *lateral* velocity variation in horizontally layered azimuthally anisotropic media. The correction term is proportional to the curvature of the zero-offset traveltime surface at the common midpoint and, therefore, can be estimated from surface seismic data. After the influence of lateral velocity variation on the effective NMO ellipses has been stripped, the generalized Dix equation can be used to compute the interval ellipses and evaluate the magnitude of azimuthal anisotropy (measured by *P*-wave NMO velocity) within the layer of interest.

This methodology was applied to a 3-D "wide-azimuth" data set acquired over a fractured reservoir in the Powder River Basin, Wyoming. The processing sequence included 3-D semblance analysis (based on the elliptical NMO equation) for a grid of common-midpoint "super-gathers," spatial smoothing of the effective NMO ellipses and zero-offset traveltimes, correction for lateral velocity variation, and generalized Dix differentiation. Our estimates of depth-varying fracture trends in the survey area, based on the interval *P*-wave NMO ellipses, are in good agreement with the results of outcrop and borehole measurements and the rotational analysis of four-component *S*-wave data.

INTRODUCTION

The azimuthal variation of normal-moveout velocity for pure (nonconverted) modes is described by an *ellipse* in the horizontal plane, even if the medium is arbitrarily anisotropic and heterogeneous (Grechka and Tsvankin, 1998). This conclusion breaks down only for rare subsurface models in which common-midpoint reflection traveltime cannot be described by a series expansion or does not increase with offset. The orientation of the normal-moveout (NMO) ellipse and the values of its semi-axes are determined by the orientation of the reflecting interface at the zero-offset reflection point and the medium properties above the reflector.

Conventional stacking-velocity analysis in 3-D surveys (e.g., those acquired using rotated swath or button-patch geometries) ignores the azimuthal dependence of normal moveout from horizontal reflectors, which may lead to distortions in seismic processing (Lynn et al., 1996). A single value of stacking (normal-moveout) velocity at a given spatial location will generally cause underestimation of NMO velocity for source-receiver azimuths near the "fast" direction and overestimation of V_{nmo} near the "slow" direction. Hence, mixing up different azimuths may impair the performance of moveout correction and the quality of the stacked section. The result of Grechka and Tsvankin (1998) makes it possible to avoid these distortions by reconstructing the best-fit NMO ellipse from the data and picking the correct stacking velocity for all azimuthal directions.

The inversion of the NMO ellipse is a much more complicated issue because the ellipticity can be caused not just by azimuthal anisotropy but also by reflector dip and lateral heterogeneity. If the medium above the reflector is horizontally homogeneous, reflector dip manifests itself through the reflection slope on the zero-offset section and can be accounted

for in the parameter-estimation procedure. Depending on the symmetry of the medium, the recovery of the anisotropic parameters in horizontally homogeneous models may require NMO ellipses measured for several different modes or reflector orientations. For instance, in orthorhombic media with a horizontal symmetry plane, the *P*-wave NMO velocity is controlled by the directions of the vertical symmetry planes, two symmetry-plane NMO velocities from a horizontal reflector, and three "anellipticity" coefficients similar to the Alkhalifah-Tsvankin (1995) parameter η for vertical transverse isotropy (Grechka and Tsvankin, 1999). All these parameters can be determined from two *P*-wave NMO ellipses recorded over an orthorhombic layer for different reflector dips and/or azimuths. Grechka and Tsvankin (1999) extended the moveout inversion to vertically inhomogeneous (i.e., horizontally stratified) orthorhombic media above a dipping reflector using the generalized Dix equation of Tsvankin et al. (1997). This methodology is also valid for the simplest azimuthally anisotropic model—transverse isotropy with a horizontal symmetry axis (HTI media), where the inversion becomes even more stable because of the smaller number of the anisotropic parameters (Contreras et al., 1999).

Reflection moveout and NMO velocity, however, are also influenced by *lateral* velocity variation that can make the azimuthal dependence of NMO velocity elliptical even for a horizontal reflector beneath an azimuthally *isotropic* medium. Since the anisotropy-induced ellipticity of the effective NMO velocity usually is relatively small (up to 10%), it may well be comparable to the distortions caused by mild lateral velocity variations. Here, we introduce a moveout correction for lateral velocity variation in horizontally layered media by using the approach of Grechka (1998) originally developed for vertical transverse isotropy (see Appendix A). The distortion of the NMO ellipse caused by lateral variation in the elastic constants turns out to be controlled by the *curvature* of the zero-offset traveltime surface at the common-midpoint (CMP) location, which can be evaluated using surface data. After removing the influence of lateral velocity variation on the effective NMO (stacking) velocity, we obtain the interval NMO ellipses from the generalized Dix equation. For such common azimuthally anisotropic models as HTI and orthorhombic media with a single vertical fracture system, the azimuth of one of the axes of the interval NMO ellipse corresponds to the fracture orientation, and the fractional difference between the semi-axes is related to the fracture density (Tsvankin, 1997a; Grechka and Tsvankin, 1999).

After discussing the theory and methodology, we present an application of our algorithm to a 3-D data set acquired by ARCO (with funding from the Gas Research Institute) over a fractured reservoir in the Powder River Basin, Wyoming. Our processing sequence made it possible to invert for the *depth-varying* fracture orientation and estimate the magnitude of azimuthal variation of *P*-wave moveout velocity over the survey area.

THEORY

Equation of the NMO ellipse

Grechka and Tsvankin (1998) considered azimuthally dependent reflection moveout of pure (nonconverted) modes around a fixed CMP location over an arbitrary anisotropic heterogeneous medium. For source-receiver offsets that do not exceed the distance between the CMP and the reflector, the reflection traveltime t in most cases can be approximated accurately by the hyperbolic equation,

$$t^2(h, \alpha) = t_0^2 + \frac{4h^2}{V_{\text{nmo}}^2(\alpha)}, \qquad (1)$$

where h is half the source-receiver offset, α is the azimuth of the CMP line, t_0 is the zero-offset traveltime, and $V_{\text{nmo}}(\alpha)$ is the normal-moveout velocity analytically defined in the zero-spread limit. Since NMO velocity is not influenced by reflection-point dispersal (Hubral and Krey, 1980, Appendix D; Grechka and Tsvankin, 1998), the hyperbolic portion of the moveout curve can be found as the sum of the *one-way* traveltimes τ from the zero-offset reflection point to the source and receiver. Under the assumption that τ is sufficiently smooth near the common midpoint to be expanded in a Taylor series in the horizontal coordinates x_1 and x_2, the azimuthally varying NMO velocity is given by (Grechka and Tsvankin, 1998)

$$V_{\text{nmo}}^{-2}(\alpha) = W_{11} \cos^2 \alpha + 2W_{12} \sin \alpha \cos \alpha + W_{22} \sin^2 \alpha, \qquad (2)$$

where the symmetric matrix $\mathbf{W}$ depends on the derivatives of τ with respect to the horizontal coordinates (x_1, x_2) as

$$W_{ij} = \tau_0 \frac{\partial^2 \tau}{\partial x_i \partial x_j}\bigg|_{\mathbf{x} = \mathbf{x}_{\text{CMP}}} = \tau_0 \frac{\partial p_i}{\partial x_j}\bigg|_{\mathbf{x} = \mathbf{x}_{\text{CMP}}},$$
$$(i, j = 1, 2). \quad (3)$$

Here $\tau_0 = t_0/2$, and (p_1, p_2) are the horizontal components of the slowness vector for rays excited at the zero-offset reflection point and recorded at the surface.

The components of the matrix $\mathbf{W}$ can be determined from surface data by means of semblance velocity analysis based on equation (2). Analytic representation of $\mathbf{W}$ [equation (3)] can then be used in the inversion of moveout data for the anisotropic parameters. Indeed, equation (3) can be converted into a relatively simple function of the slowness components of the zero-offset ray. This allows one to find $\mathbf{W}$ for a given anisotropic model directly from the Christoffel equation and build an efficient parameter-estimation scheme (Tsvankin et al., 1997). Contreras et al. (1999) applied this formalism to invert azimuthally dependent *P*-wave NMO velocities (i.e., the matrices $\mathbf{W}$) of horizontal and dipping events for the parameters of HTI media.

To show that the azimuthal variation in NMO velocity is elliptical, we introduce the angle

$$\beta = \tan^{-1}\left[\frac{W_{22} - W_{11} + \sqrt{(W_{22} - W_{11})^2 + 4W_{12}^2}}{2W_{12}}\right]$$
$$(W_{12} \neq 0) \quad (4)$$

that corresponds to one of the principal directions of the matrix $\mathbf{W}$. Expressing $\mathbf{W}$ in terms of its eigenvalues

$$\lambda_{1,2} = \frac{1}{2}\left[W_{11} + W_{22} \pm \sqrt{(W_{11} - W_{22})^2 + 4W_{12}^2}\right] \qquad (5)$$

and the angle β, we can rewrite equation (2) as

$$V_{\text{nmo}}^{-2}(\alpha) = \lambda_1 \cos^2(\alpha - \beta) + \lambda_2 \sin^2(\alpha - \beta). \quad (6)$$

Unless reflection traveltime decreases with offset in some directions leading to reverse moveout (i.e., $V_{\text{nmo}}^2 < 0$, which implies that $\lambda_1 < 0$ and/or $\lambda_2 < 0$), equation (6) describes an *ellipse* in the horizontal plane (Grechka and Tsvankin, 1998). The NMO velocities in the directions of the elliptical axes (we denote them $v_{e\ell 1}$ and $v_{e\ell 2}$) can be expressed through the eigenvalues as

$$v_{e\ell 1} = 1/\sqrt{\lambda_1} \quad \text{and} \quad v_{e\ell 2} = 1/\sqrt{\lambda_2}. \quad (7)$$

Generalized Dix equation

If the model consists of a stack of horizontal homogeneous layers above a dipping reflector, NMO velocity can be found analytically from the generalized Dix equation of Tsvankin et al. (1997). The matrix $\mathbf{W}(L)$ [equation (3)] that defines the NMO ellipse (2) for reflection from the bottom of layer L can be expressed through a Dix-type average of the inverse interval matrices $\mathbf{W}_\ell$ weighted by the interval zero-offset traveltimes τ_ℓ as

$$\mathbf{W}^{-1}(L) = \frac{1}{\sum\limits_{\ell=1}^{L} \tau_\ell} \sum_{\ell=1}^{L} \tau_\ell \mathbf{W}_\ell^{-1}. \quad (8)$$

To solve equation (8) for the interval quantities, it can be rewritten in the Dix-type differentiation form:

$$\mathbf{W}_\ell^{-1} = \frac{\tau(\ell)\mathbf{W}^{-1}(\ell) - \tau(\ell - 1)\mathbf{W}^{-1}(\ell - 1)}{\tau(\ell) - \tau(\ell - 1)}. \quad (9)$$

The matrices $\mathbf{W}(\ell - 1)$ and $\mathbf{W}(\ell)$ describe the effective NMO ellipses for reflections from the top and the bottom of the ℓth layer; $\tau(\ell - 1)$ and $\tau(\ell)$ are the corresponding zero-offset traveltimes. Equation (9) allows one to calculate the matrix $\mathbf{W}_\ell$ that determines the interval NMO ellipse in the ℓth layer.

Equations (8) and (9) represent a 3-D generalization, for arbitrary anisotropic media, of the well-known Dix (1955) formula. The interval matrices $\mathbf{W}_\ell$ in equation (3) are computed for the horizontal components of the slowness vector of the zero-offset ray. If the reflectors are *dipping* and the zero-offset slowness directions are not vertical, the matrices $\mathbf{W}(\ell)$ and $\mathbf{W}^{-1}(\ell - 1)$ determined from the data will generally correspond to slowness vectors with *different* horizontal components (Tsvankin et al., 1997). As a result, layer-stripping by means of equation (9) involves recalculating each interval matrix $\mathbf{W}_\ell$ from one value of the slowness vector to another. This problem, however, does not arise for horizontal reflectors, because in this case the horizontal slowness components are equal to zero for all reflection events.

It should be emphasized that equation (9) cannot be used if the horizontal components of the slowness vector vary along the one-way ray under the influence of lateral heterogeneity and/or dipping (or irregular) interfaces above the ℓth reflector. For these laterally heterogeneous models, Hubral and Krey (1980) suggested implementing the Dix-type differentiation using the downward continuation of the wavefront curvature associated with the zero-offset ray. In principle, this methodology

can be generalized to construct the effective NMO ellipses in anisotropic heterogeneous media (Tsvankin et al., 1997). However, such an approach involves numerical ray tracing through heterogeneous anisotropic models; also, the downward continuation requires knowledge of the medium parameters in the overburden. Note that the numerical solution is required even for relatively simple isotropic models containing homogeneous layers separated by curved interfaces (Hubral and Krey, 1980).

Influence of weak lateral heterogeneity on NMO ellipses

The discussion above suggests that reconstruction of the interval NMO ellipses in heterogeneous anisotropic media is impossible without determination of the properties of the overburden and employing numerical algorithms. The only way to preserve the relative simplicity of the Dix differentiation [equation (9)] in the presence of lateral heterogeneity is to impose certain restrictions on the model complexity. We implement this approach below by assuming that the medium consists of horizontal layers with weak lateral velocity variation.

Horizontal layer with lateral velocity variation.—Let us consider the simplest model of a single anisotropic layer above a horizontal reflector. We assume that the horizontal plane is a plane of symmetry, which implies that the medium may be monoclinic, orthorhombic, or transversely isotropic with a vertical or horizontal symmetry axis. In general, the type of symmetry may change laterally provided the slowness surface remains symmetric with respect to the horizontal plane.

Suppose the NMO ellipse (2) for the reflection from the bottom of the reference *homogeneous* layer (with the same parameters as at the CMP location) is described by a matrix denoted as $\mathbf{W}^{\text{hom}}$ [equation (3)]. In accordance with the general result of Grechka and Tsvankin (1998), the azimuthal variation of NMO velocity in the presence of lateral velocity variation remains elliptical, but the corresponding matrix $\mathbf{W}$ is different ($\mathbf{W}^{\text{het}}$). Assuming that lateral velocity variation (or lateral heterogeneity, "LH") is weak on the scale of the CMP gather and retaining only linear terms in the spatial derivatives of the velocity function yields the following relationship between the two NMO ellipses (Appendix A)

$$W_{ij}^{\text{het}} = W_{ij}^{\text{hom}} - \frac{\tau_0^2}{3 V_0} \left.\frac{\partial^2 V_0}{\partial y_i \partial y_j}\right|_{\mathbf{y}=\mathbf{y}_{\text{CMP}}}, \quad (i, j = 1, 2),$$
$$(10)$$

where $\tau_0 = \tau_0(\mathbf{y})$ is the one-way zero-offset (vertical) traveltime, and $V_0 = V_0(\mathbf{y})$ is the vertical velocity at the CMP location $\mathbf{y} = (y_1, y_2)$. Equation (10) indicates that, in the linear approximation employed here, the influence of lateral velocity variation on the NMO ellipse is proportional to the *curvature* of the vertical-velocity surface $V_0(\mathbf{y})$ at the common midpoint.

If the reflector possesses dip (ignored here), equation (10) will also contain the first spatial derivatives of the velocity $V_0(\mathbf{y})$. These derivatives, however, make a noticeable contribution only for substantial dips ϕ because they are multiplied with the cubic and higher powers of $\sin \phi$ (Grechka and Cohen, 1996). In the case study discussed below, the dips are on the order of the first few degrees, and equation (10) is sufficiently accurate. Correction for lateral velocity variation in dipping layers will be treated in sequel publications.

Figure 1 displays a numerical test of equation (10) for a transversely isotropic medium with a horizontal symmetry axis parallel to the axis y_1. Ray-traced P-wave reflection traveltimes were computed at a common-mipoint $y_1 = y_2 = 0$ for two anisotropic models: an HTI layer with laterally varying vertical velocity and a reference homogeneous HTI layer with the parameters corresponding to the CMP location (Figure 1a). After calculating the traveltime along four differently oriented CMP lines, we used the hyperbolic moveout equation (1) to obtain azimuthally dependent NMO velocity and reconstruct the NMO ellipses for both the homogeneous and LH layers (Figure 1b). The difference between the two ellipses can be understood by analyzing the saddle-shaped velocity surface $V_0(\mathbf{y})$ in Figure 1a. The positive curvature of $V_0(\mathbf{y})$ in approximately y_2 direction (Figure 1a) increases the velocity for rays propagating in this direction and, therefore, leads to a higher NMO velocity for azimuths close to 90° (Figure 1b). Likewise, there is a small decrease in the NMO velocity at azimuths near 0° because of the negative curvature of $V_0(\mathbf{y})$ in the y_1-direction.

To test the analytic correction for lateral velocity variation, we calculated the derivatives $\partial^2 V_0/\partial y_i \partial y_j$ at the CMP location and used equation (10) with the exact expression for W_{ij}^{hom} to obtain W_{ij}^{het} and the NMO velocity in the LH layer. This analytic NMO ellipse (solid line in Figure 1b) is virtually identical to the one generated numerically (dotted line), with the maximum difference less than 0.5%. Note that the quasi-linear increase in vertical velocity in the y_1-direction (Figure 1a) has almost no influence on NMO velocity that is controlled by the curvature of $V_0(\mathbf{y})$ at the common midpoint. This observation agrees with the result of Grechka (1998) who proved that NMO velocity for vertical transverse isotropy is independent of constant lateral velocity gradient (in the linear approximation).

Even though equation (10) provides an adequate approximation for the NMO ellipse in an LH layer, it is difficult to use in reflection data processing because the vertical velocity V_0 in anisotropic media cannot be determined from P-wave reflection traveltimes. [The only exception is the HTI model in

which one of the semi-axes of the NMO ellipse is equal to the true vertical velocity (Tsvankin, 1997a; Contreras et al., 1999).] However, since the layer is horizontal and $V_0\tau_0 = \text{const}$, the spatial derivatives of the vertical velocity V_0 can be replaced with those of the vertical traveltime τ_0. Differentiating $V_0\tau_0$ twice with respect to y_i and y_j yields

$$\frac{\partial^2 V_0}{\partial y_i \partial y_j}\tau_0 + \frac{\partial^2 \tau_0}{\partial y_i \partial y_j}V_0 = 0. \qquad (11)$$

Terms $(\partial V_0/\partial y_i)(\partial \tau_0/\partial y_j)$ were dropped from equation (11) because they are quadratic in the small quantities related to LH. Substituting equation (11) into equation (10) gives the following representation of $\mathbf{W}^{\text{hom}}$:

$$W_{ij}^{\text{hom}} = W_{ij}^{\text{het}} - \frac{\tau_0}{3}\frac{\partial^2 \tau_0}{\partial y_i \partial y_j}\bigg|_{\mathbf{y}=\mathbf{y}_{\text{CMP}}}, \qquad (i, j = 1, 2). \qquad (12)$$

Note that all terms on the right-hand side of equation (12) can be found from the traveltimes of a given reflection event recorded over an area around the CMP location. Evaluating the second derivative of the vertical traveltime usually requires smoothing the function $\tau_0(y_1, y_2)$; this is discussed in more detail in the section devoted to the case study.

Two layers with lateral velocity variation.—The methodology discussed in the previous section can be extended to the reflector beneath any number of horizontal anisotropic layers with a horizontal symmetry plane. For multilayered media, however, we assume that not only lateral velocity variation, but also azimuthal anisotropy is weak. Without the latter assumption, the correction term involves the interval vertical velocities that cannot be found from reflection data.

If the model consists of two horizontal layers, the NMO ellipse for the reflection from the bottom of the second layer can
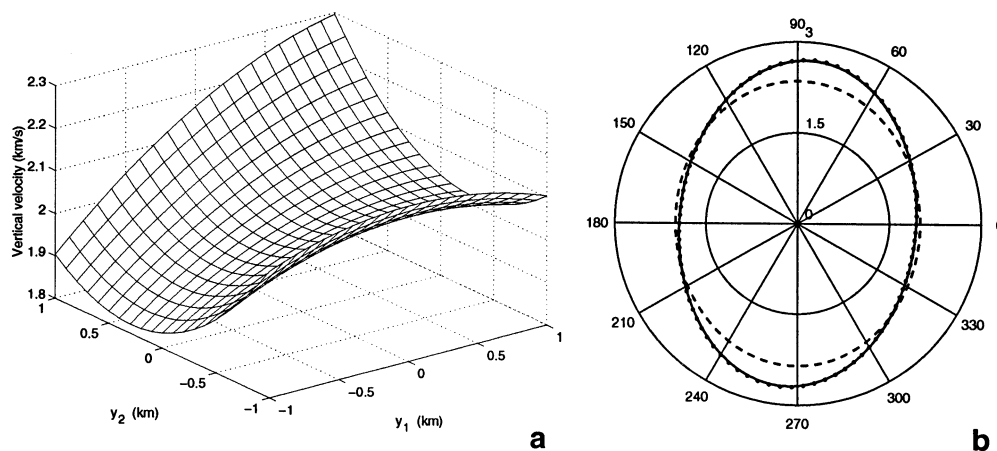

a   **b**

FIG. 1. (a) Lateral variation of the vertical velocity in an HTI layer with the symmetry axis parallel to the y_1-direction. (b) NMO ellipses: dashed—for a homogeneous HTI layer, dotted and solid—for an HTI layer with lateral velocity variation shown on the left. The dotted NMO ellipse is reconstructed from ray-traced traveltimes on a speadlength equal to the thickness of the layer (1.75 km), the solid one is obtained from the NMO ellipse in the homogeneous HTI layer using equation (10). The generic Thomsen (1986) parameters of the medium (defined with respect to the symmetry axis) are $\epsilon = 0$, $\delta = 0.2$. Azimuth 0° corresponds to the y_1-axis in Figure 1a.

be represented as (Appendix B)

$$W_{ij}^{\text{hom}} = W_{ij}^{\text{het}} - \frac{\tau_0}{3}\left[k^2\frac{\partial^2\tau_0}{\partial y_i\partial y_j} + (1+k)\frac{\partial^2\tau_{01}}{\partial y_i\partial y_j}\right],$$
$$(i, j = 1, 2), \quad (13)$$

with

$$k = 1 - \frac{\tau_{01}V_{\text{cir1}}^2}{\tau_0 V_{\text{cir}}^2}. \quad (14)$$

Here τ_{01} and τ_0 are the one-way zero-offset traveltimes for the reflections from the bottom of the first and the second layer, respectively; all derivatives are evaluated at the CMP location $\mathbf{y} = \mathbf{y}_{\text{CMP}}$. V_{cir1} and V_{cir} are the "circular" approximations of the NMO ellipses for the reflections from the bottom of the first and second layer (V_{cir1} coincides with the interval value $V_{\text{cir}}^{(1)}$ introduced in Appendix B). They are obtained by averaging the azimuthally dependent NMO velocity [equation (2)] over all azimuths as

$$V_{\text{cir}}^{-2} = \frac{1}{2\pi}\int_0^{2\pi} V_{\text{nmo}}^{-2}(\alpha)\,d\alpha = \frac{W_{11}^{\text{het}} + W_{22}^{\text{het}}}{2}. \quad (15)$$

To examine how the lateral velocity variation in a certain interval contributes to the overall correction term in equation (13), we consider a model with a laterally homogeneous upper layer, i.e.,

$$\frac{\partial^2\tau_{01}}{\partial y_i\partial y_j} = 0. \quad (16)$$

In this case, equation (13) simplifies to

$$W_{ij}^{\text{hom}} = W_{ij}^{\text{het}} - \frac{k^2\tau_0}{3}\frac{\partial^2\tau_0}{\partial y_i\partial y_j}, \quad (i, j = 1, 2). \quad (17)$$

Therefore, as could be expected, the correction caused by the lateral velocity variation becomes smaller if we add a laterally homogeneous layer on top of an LH layer. Indeed, the difference between the correction terms in equation (17) and in the single-layer equation (12) is in the factor $k^2 = (1 - \tau_{01}V_{\text{cir1}}^2/\tau_0 V_{\text{cir}}^2)^2$, which is always smaller than unity. More importantly, equation (17) shows that, if $V_{\text{cir1}}^2 = V_{\text{cir}}^2$, the correction for LH is proportional to the *squared* relative thickness of the LH layer. If, for example, the relative thickness of the LH layer $[(\tau_0 - \tau_{01})/\tau_0]$ is equal to 0.5, the term $(1 - \tau_{01}/\tau_0)^2$ goes down to 0.25 ($k^2 = 0.25$) compared to unity for a single layer. Such a nonlinear dependence means that the influence of an LH layer with a fixed thickness on the effective NMO ellipse decreases rapidly with the layer's depth. This fact can be explained by considering the lateral position of reflected rays in a CMP gather: as the LH layer moves deeper, the rays crossing it sample a smaller vicinity of the common midpoint and, therefore, are less dependent on the lateral velocity variation.

FIELD-DATA EXAMPLE

The correction for lateral velocity variation combined with the generalized Dix formula provides an analytic basis for interval moveout velocity analysis in arbitrary anisotropic media. We tested the formalism described above on a 3-D data set acquired for purposes of fracture detection by ARCO (with funding from the Gas Research Institute) in the Powder

River Basin, Wyoming. This survey was designed using a button-patch geometry to provide full azimuthal coverage in the conventional range of source-receiver offsets. To enhance the signal-to-noise ratio, the data were collected into 169 "superbins,"[1] each with a somewhat random distribution of azimuths and offsets; a typical superbin is shown in Figure 2. A description of the geology of the area, data acquisition, and preliminary processing results can be found in Corrigan et al. (1996) and Withers and Corrigan (1997).

Our main goal was to recover the interval P-wave NMO ellipses associated with azimuthal anisotropy and use them to characterize the laterally varying fracturing in different subsurface layers. The processing flow included the following main steps:

1) 3-D semblance analysis to obtain the effective NMO ellipses for each superbin;
2) Spatial smoothing of the effective NMO ellipses;
3) Correction of the effective NMO ellipses for lateral velocity variation;
4) Generalized Dix-type layer stripping to obtain the interval NMO ellipses.

Below, we describe each processing step in more detail and discuss our final results.

3-D semblance analysis

First, it was necessary to find the effective NMO ellipses for reflections from the most prominent boundaries over the survey area. There are at least two possible ways of performing moveout velocity analysis of 3-D multi-azimuth P-wave reflection data and obtaining the effective NMO ellipses. First, one can divide the data for a given superbin into several azimuthal sectors and perform conventional hyperbolic velocity
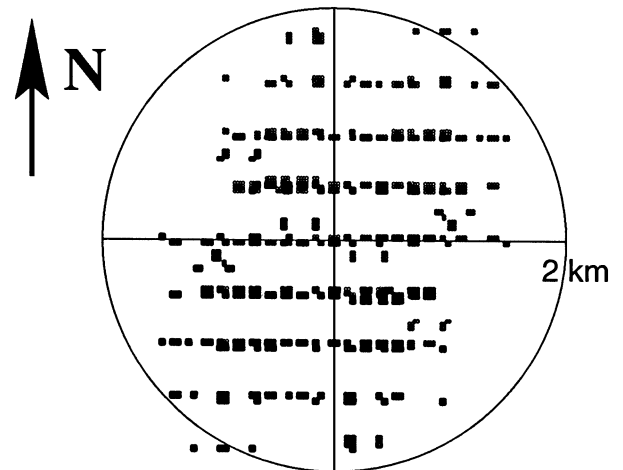
FIG. 2. Plan view of the source and receiver positions (dots) for a single superbin. The superbin contains approximately 400 source-receiver pairs with the common-midpoint scatter of up to about 80 m (2% of the maximum offset). The maximum offset is approximately equal to the depth of the deepest reflector.

[1]A composite CMP gather that includes all source-receiver pairs with close midpoints.

analysis for source-receiver pairs within each sector. Then, the best-fit moveout (stacking) velocity $V_{nmo}(\alpha)$ for a given reflector is determined by approximating the moveout-velocity measurements with an ellipse using equation (2). While azimuthal sectoring makes it possible to use conventional software for semblance analysis, we found that the number and size of the sectors may influence the results of the velocity estimation because the distribution of offsets and azimuths is not completely random.

Therefore, we implemented another approach by treating all azimuths simultaneously and performing semblance analysis for the whole superbin at each zero-offset time τ_0. This "global" semblance analysis is based on the hyperbolic moveout equation (1) and requires scanning over the three components of the matrix **W** responsible for the NMO ellipse [equation (2)]. Note that since the maximum offset was a little smaller than the depth of the basement (the deepest reflector), the moveout for all superbins was close enough to hyperbolic.

To make this search more efficient and avoid the full-scale 3-D semblance scan, we use an equivalent representation of the NMO ellipse (2) in terms of the average velocity V_{cir} [equation (15)] and two dimensionless quantities, e_1 and e_2:

$$V_{nmo}^{-2}(\alpha) = V_{cir}^{-2}(1 + e_1 \cos 2\alpha + e_2 \sin 2\alpha), \qquad (18)$$

where the parameters e_1 and e_2 control the deviation of the NMO ellipse from an average "NMO circle." Combining equations (2), (15), and (18) yields

$$e_1 = \frac{W_{11} - W_{22}}{W_{11} + W_{22}} \quad \text{and} \quad e_2 = \frac{2 W_{12}}{W_{11} + W_{22}}. \qquad (19)$$

Although both equation (18) and the original NMO ellipse (2) contain three unknown parameters, the introduction of e_1 and e_2 allows us to speed up the semblance analysis by dividing it into two stages. Indeed, the NMO ellipses are not far different from a circle, and e_1 and e_2 are small compared to unity, if azimuthal anisotropy is relatively weak and the reflectors are subhorizontal (a common case). Therefore, at first we assume $e_1 = e_2 = 0$ and carry out a conventional 1-D scan over V_{cir}. This procedure, routinely applied in 3-D processing, ignores the azimuthal dependence of NMO velocity and yields an average NMO circle that can be considered as an initial guess for the NMO ellipse. Then the coefficients e_1 and e_2 are obtained by deforming the circle into the best-fit NMO ellipse (18) that provides the highest value of semblance. This search is performed by an efficient minimization technique [Powell's method, see Press et al. (1987)] that usually converges in 5–10 iterations, making an extensive 3-D semblance scan unnecessary.

Figure 3 shows typical semblance curves obtained from the conventional and azimuthal velocity analysis for one of the superbins. (By conventional velocity analysis we mean the first stage of our semblance search that provides the best-fit azimuthally independent velocity V_{cir}.) While the two curves are close to each other over most of the time interval (i.e., the NMO ellipses are close to a circle), for the reflections at the vertical times of 1.54 s, 1.84 s and, especially, 2.57 s, the azimuthal velocity analysis improves the fit to moveout and provides higher semblance values. For these reflection events, the conventional algorithm smears the azimuthal velocity varia-

tions and produces a distorted value of moveout velocity for any given azimuth, thus leading to a lower quality of stack. And, of course, conventional moveout analysis cannot be used to extract information about azimuthal anisotropy from reflection traveltimes.

According to Withers and Corrigan (1997), the reflection at a two-way vertical time of 2.14 s corresponds to the bottom of the Frontier/Niobrara formations, and the event at 2.57 s is the basement reflection. The producing fractured reservoir (the main target of the survey) covers the time interval approximately between 1.84 s and 2.14 s.

The results of the azimuthal velocity analysis for reflections marked in Figure 3 over the whole survey area are shown in Figure 4. Each tick corresponds to the effective NMO ellipse at a certain superbin. The direction of a tick indicates the azimuth of the semi-major axis of the NMO ellipse, while the tick's length is proportional to the ellipticity e (i.e., the elongation of the NMO ellipse). We define e as the fractional difference between the semi-axes $v_{e\ell2}$ and $v_{e\ell1}$ [equation (7)] to obtain

$$e = 2\frac{v_{e\ell2} - v_{e\ell1}}{v_{e\ell2} + v_{e\ell1}}. \qquad (20)$$

The maximum value of e for the whole survey area does not exceed 0.05. We will see, however, that the *interval* NMO ellipses in certain layers may have much higher values of e. The ellipticity patterns in Figure 4 are sufficiently close to the results of Withers and Corrigan (1997), who used a somewhat different (interactive) algorithm for azimuthal velocity analysis of this data set.

Smoothing of the effective NMO ellipses

An important issue to contemplate is to what extent we can trust the rapid lateral variations in the parameters of the NMO ellipses in Figure 4. Note that the size of the whole survey area is not far different from the maximum offset for a single superbin (compare the scales in Figures 2 and 4). This means that the reflected rays corresponding to adjacent superbins propagate
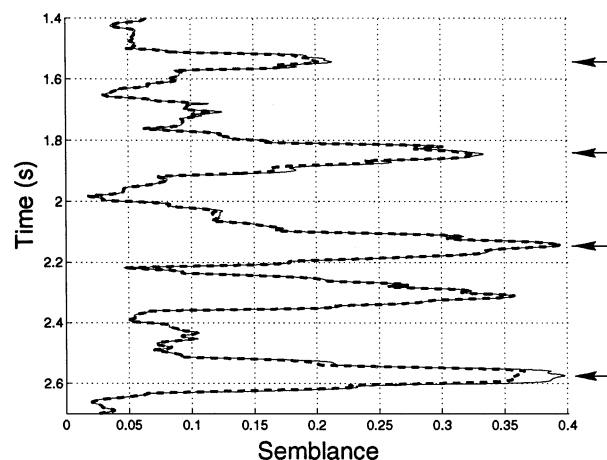

FIG. 3. Semblance curves obtained by the conventional velocity analysis that ignores the azimuthal dependence of moveout velocity (dashed) and by our azimuthal velocity analysis (solid). Arrows indicate the reflections used in the generalized Dix differentiation.

through almost the same subsurface volume. Hence, a 90° rotation of the semi-major axis of the NMO ellipse between adjacent superbins [e.g., between the point with the crossline coordinate $y_1 = 0.6$ km and inline coordinate $y_2 = 2.0$ km and an adjacent point $\mathbf{y} = (0.6, 2.2)$ km in Figure 4d] is most likely caused by noise in input data that leads to errors in azimuthal velocity analysis. Clearly, reliable estimation of the interval ellipticities is impossible without spatial smoothing of the effective NMO ellipses.

Our design of the smoothing procedure is based on the size of the first Fresnel zone at the reflector that was estimated for

the central frequency in the data. Figure 5 shows that the whole survey area is only about 6–7 times larger than the area of the Fresnel zone computed for the deepest reflector. Since it is reasonable to assume that each Fresnel zone can yield a single NMO ellipse, no more than 6–7 independent ellipses can be obtained for the whole area. Therefore, the spatial variation in the smoothed matrix $\mathbf{W}^{\mathrm{het}}(\mathbf{y})$ should be represented by a function with 6–7 independent parameters. In essence, by applying spatial smoothing we suppress high-frequency spatial variations in the NMO velocity that cannot be resolved from the data.
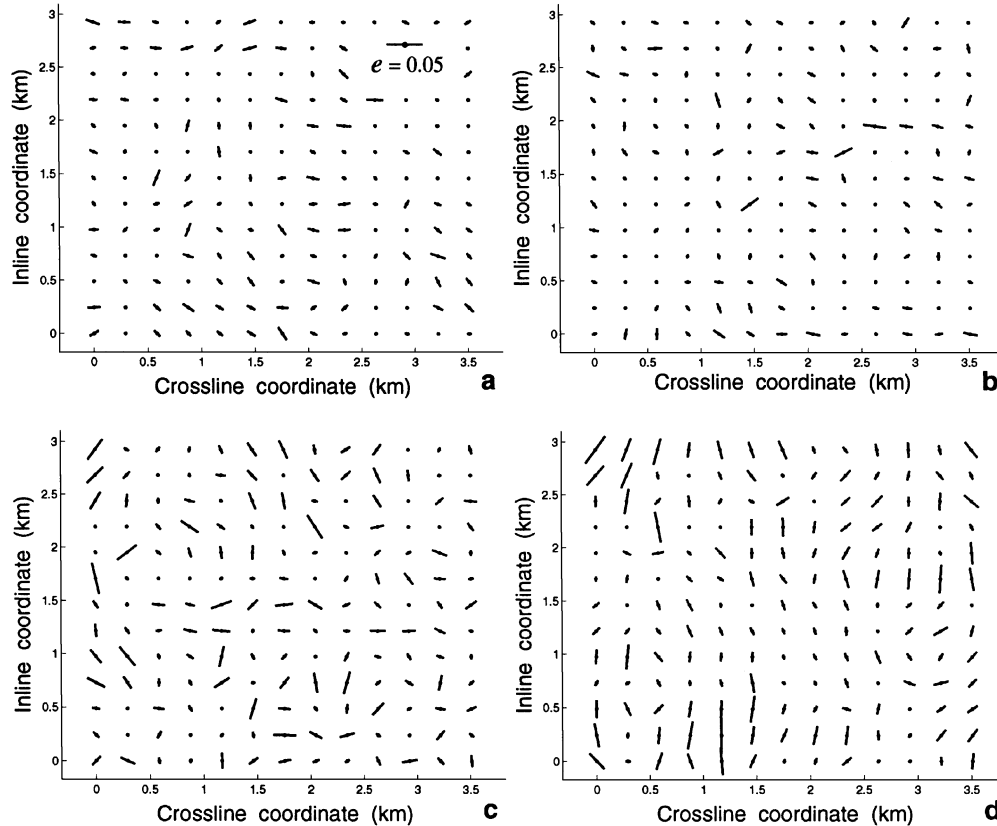

FIG. 4. Raw effective ellipticities for reflections at 1.54 s (a), 1.84 s (b), 2.14 s (c), and 2.57 s (d).
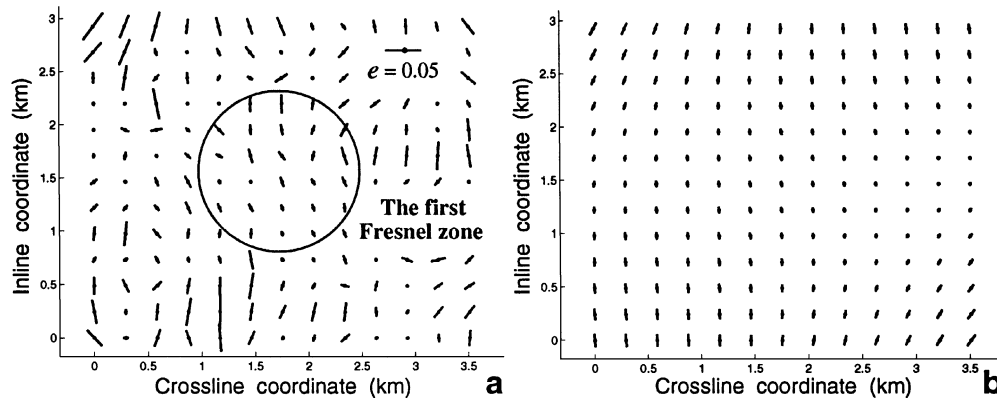

FIG. 5. (a) Raw effective ellipticities for the reflection at a vertical time of 2.57 s with a circle corresponding to the first Fresnel zone at the reflector. (b) The effective ellipticities from Figure 5a after smoothing.

Thus, we seek $\mathbf{W}^{\text{het}}(\mathbf{y})$ as a quadratic polynomial

$$W_{ij}^{\text{het}}(y_1, y_2) = \sum_{k,l=0}^{k+l \leq 2} \mathcal{W}_{ij}^{(kl)} y_1^k y_2^l, \qquad (i, j = 1, 2), \quad (21)$$

where the six coefficients $\mathcal{W}_{ij}^{(kl)}$ (for each element W_{ij} of the matrix $\mathbf{W}^{\text{het}}$) are found by least-squares fitting of equation (21) to the raw NMO ellipses from Figure 4. The choice of the quadratic polynomial (21) means that the NMO ellipses are approximated with surfaces $\mathbf{W}^{\text{het}}(\mathbf{y})$ of constant curvature over the whole survey area.

The effective ellipticities after the spatial smoothing are displayed in Figures 5b and 6. The smoothing led to an overall decrease in the magnitude of azimuthal NMO-velocity variation for the events at 1.54, 1.84, and 2.14 s. For the deepest reflection at 2.57 s, the smoothed ellipticity is more substantial and has a predominant north-south orientation. The results of smoothing indicate that the level of errors in picking azimuthally dependent NMO velocities is about 1–2%, and small effective ellipticities on the order of 2%, quite common for all reflection events, may not carry useful information about the fracture direction.

Correction for lateral velocity variation

The formalism of Grechka and Tsvankin (1998) shows that the effective ellipticities in Figure 6 may be caused by the following three factors:

1) reflector dip;
2) lateral heterogeneity above the reflector;
3) azimuthal anisotropy.

Correcting for the influence of reflector dip and lateral heterogeneity is a crucial problem in fracture characterization using azimuthal moveout analysis. Below, we demonstrate that the reflector dips in the area are negligibly small, and the subsurface model can be represented adequately by a stack of horizontal layers. Then, we use the analytic expressions developed above [equations (12)–(14)] to correct the effective NMO ellipses for lateral velocity variation. Applicability of our approximations, based on the assumption of weak lateral velocity variation and weak anisotropy, is justified by the fact that the effective ellipticity is relatively small (Figure 6), and, therefore, all factors responsible for it have to be small as well.

Figure 7 shows smoothed surfaces of the two-way, zero-offset reflection traveltime $t(\mathbf{y}) = 2\tau_0(\mathbf{y})$ for the four reflection events. The smoothing function had the same form as the one used for NMO ellipses [equation (21)]. The maximum apparent dip in Figure 7 reaches 30–40 ms over a distance of about 3 km, giving an apparent horizontal slowness $p = \frac{1}{2} dt/dy$ of about 0.005 s/km. Attributing this spatial variation in the zero-offset time to reflector dip ϕ yields the relative correction in the NMO velocity that can be estimated roughly (in the isotropic limit) as $(1/\cos\phi - 1) \approx (1/\sqrt{1 - p^2 V_{\text{cir}}^2} - 1)$. Substituting $p = 0.005$ s/km and $V_{\text{cir}} = 4.0$ km/s (see Figure 8), we find that the distortion caused by reflector dip is close to just 0.02% of V_{cir}. This distortion is an order of
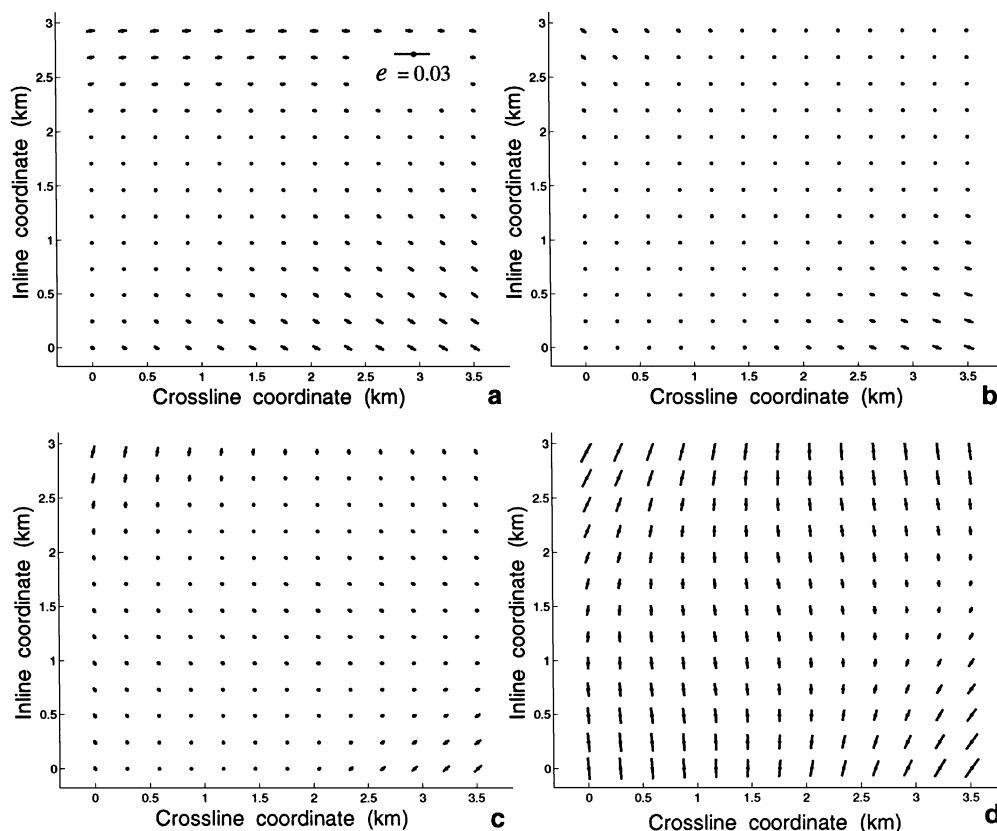

FIG. 6. Smoothed effective ellipticities for the reflections at 1.54 s (a), 1.84 s (b), 2.14 s (c), and 2.57 s (d).
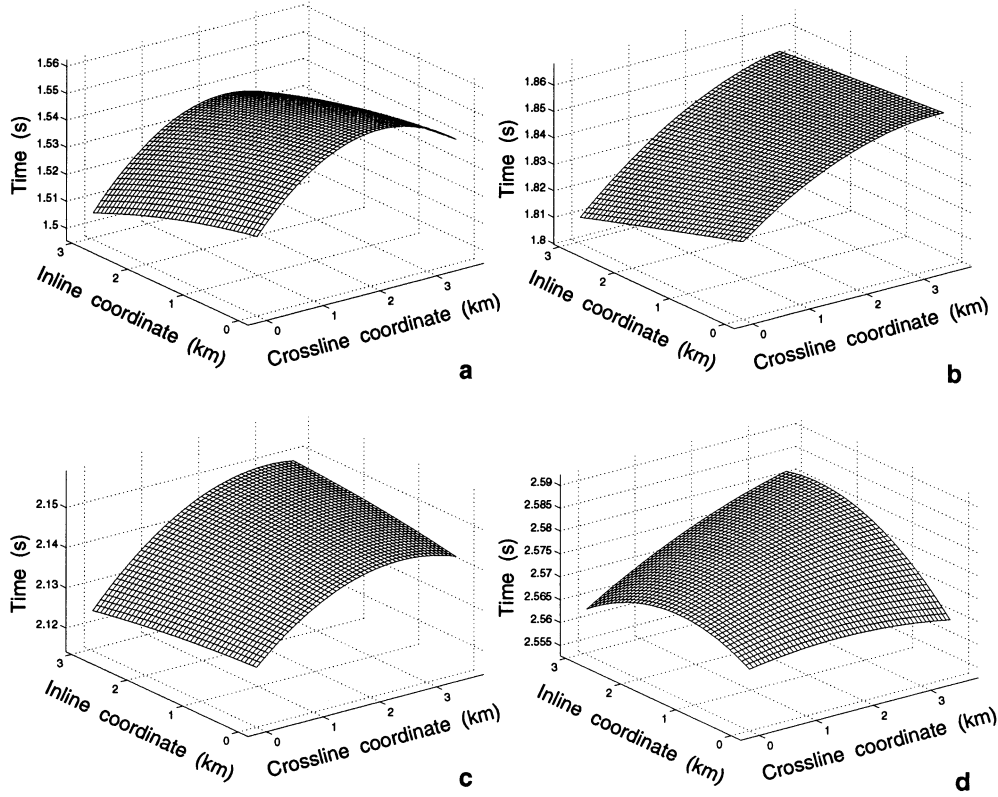
FIG. 7. Smoothed two-way zero-offset traveltime surfaces for the reflections at 1.54 s (a), 1.84 s (b), 2.14 s (c), and 2.57 s (d).
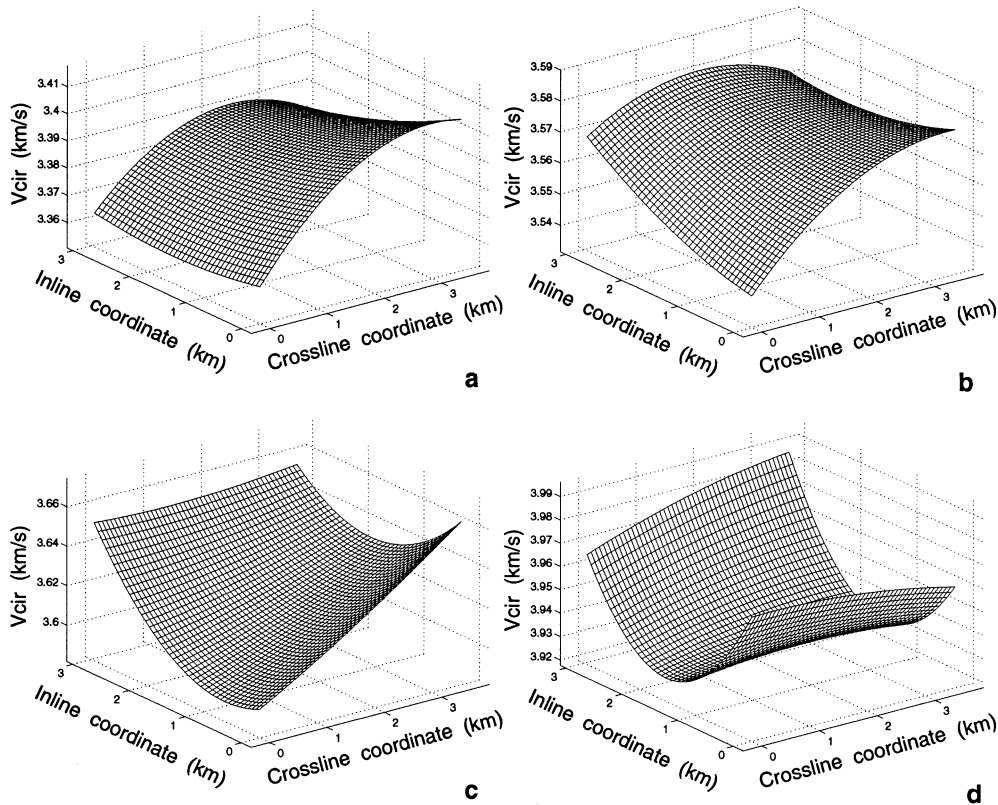

FIG. 8. Smoothed average effective NMO velocities V_{cir} [equation (15)] for the reflections at 1.54 s (a), 1.84 s (b), 2.14 s (c), and 2.57 s (d).

magnitude smaller than the estimated errors in the effective NMO ellipses. Even though the apparent dip of the zero-offset traveltime surface is also influenced by lateral velocity variation (Figure 8), it is clear that the contribution of dip to NMO velocity can be ignored for all reflection events. The absence of dip enables us to correct for lateral velocity variation using the theory for horizontally layered media developed above.

The zero-offset traveltime surfaces $t(\mathbf{y})$ (Figure 7), together with the surfaces of the average NMO velocity $V_{\text{cir}}(\mathbf{y})$ shown in Figure 8, can be used to strip the influence of lateral velocity variation from the effective NMO ellipses. Note that the curvature of the traveltime surface, responsible for the influence of lateral velocity variation on the NMO ellipse, is directly determined by the coefficients of our smoothing function [equation (21)] and remains constant over the survey area. The correction for lateral velocity variation for the shallow reflection (at 1.54 s) was carried out using the single-layer equation (12), while for the event at 1.84 s we applied the two-layer equation (13). In principle, the two deepest events (at 2.14 s and 2.57 s) should be treated by means of a more complicated multiple-layer correction formula (not given here). However, to simplify the processing algorithm, we used the same equation (13) for both deeper reflections under the assumption that the whole stratified overburden may be described as a single effective layer. For instance, in calculating the correction term for the basement reflection (2.57 s), the first-layer parameters in equation (13) (τ_{01} and V_{cir1}) were assumed to correspond to the event at 2.14 s.

Comparing the corrected NMO ellipses in Figure 9 with the input ones in Figure 6 illustrates the distortions caused by lateral velocity variation in the azimuthal dependence of NMO velocity. As an example, for the event at 1.54 s the surface $t(\mathbf{y})$ has a *negative* curvature in approximately the east-west, or crossline, direction (Figure 7a). Hence, the lateral velocity variation leads to an increase in the NMO velocity in the east-west azimuth [see equation (12)], making the uncorrected NMO ellipses in Figure 6a almost circular. By removing the influence of lateral velocity variation, we produce the ellipses extended in the orthogonal (south-north) direction, thus restoring the signature caused by the azimuthal anisotropy (Figure 9a). For the other three reflections, the interpretation of the results becomes more complicated because the correction term involves two traveltime surfaces (τ_0 and τ_{01}).

It should be emphasized that the correction for lateral velocity variation is highly sensitive to the shape of the surfaces $t(\mathbf{y})$. Since these surfaces are supposed to be differentiated twice [see equations (12) and (13)], the form of the smoothing function can change the corrected NMO ellipse substantially. We attempted to reduce the degree of smoothing of NMO ellipses by using a bi-cubic polynomial [$k + \ell \leq 3$ in equation (21)] or the running average over the area of the first Fresnel zone (see Figure 5). In both cases, we obtained unrealistic large values of the corrected effective ellipticity (exceeding 0.3), which is indicative of overfitting the data and amplifying errors in the raw NMO ellipses.

Generalized Dix differentiation of the effective NMO ellipses

After removing the influence of lateral velocity variation, we can perform the last step of our processing sequence—apply
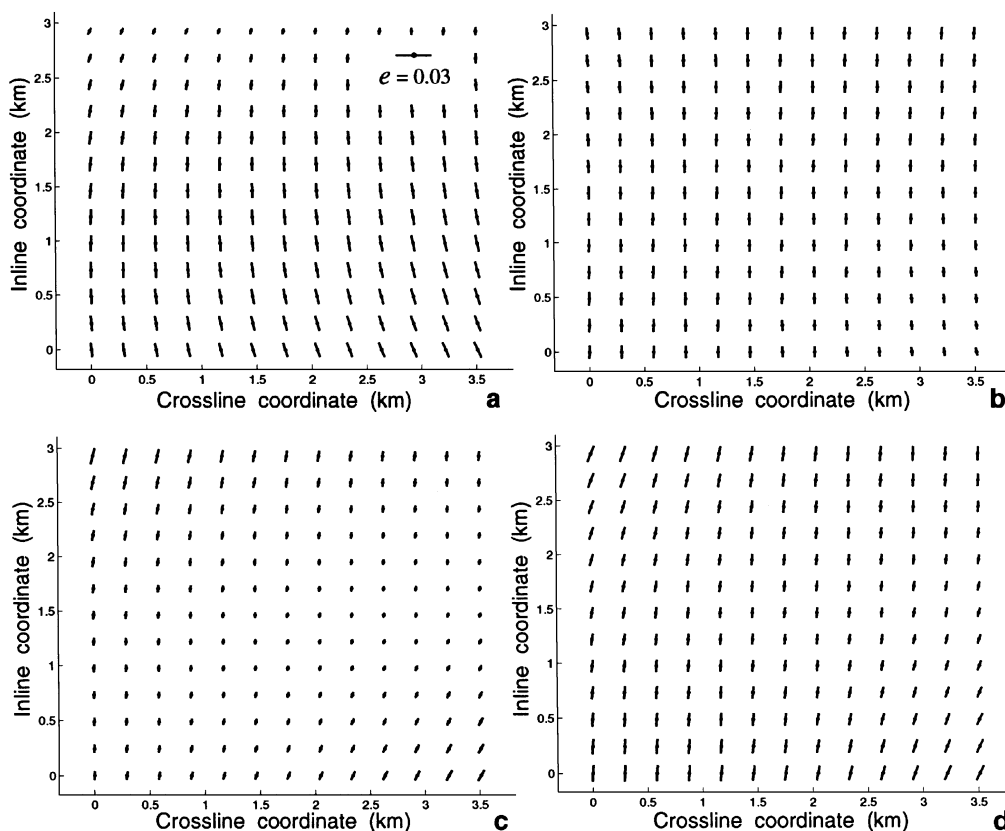

FIG. 9. Effective ellipticities corrected for lateral velocity variation for the reflections at 1.54 s (a), 1.84 s (b), 2.14 s (c), and 2.57 s (d).

the generalized Dix equation (9) to the effective ellipticities (Figure 9) and obtain the interval NMO ellipses (Figure 10). Azimuthal variation in the interval NMO velocity in Figure 10 is associated exclusively with azimuthal anisotropy and, therefore, carries information about fracturing. Assuming that each layer contains a single set of vertical fractures in an isotropic or vertical transversely isotropic (VTI) matrix, which is consistent with the available geologic information (Corrigan et al., 1996; Withers and Corrigan, 1997), the azimuth of the semimajor axis of the NMO ellipse gives the fracture orientation (i.e., NMO velocity reaches its maximum in the fracture direction), while the ellipticity e is related to the fracture density (Tsvankin, 1997a).

In the layer between 1.54 s and 1.84 s, the semi-major axis of the NMO ellipse is predominantly oriented east-west, but the ellipticity is rather small—up to 3% (Figure 10a). The pattern changes significantly in the producing interval between 1.84 and 2.14 s. The azimuth of the NMO ellipse varies substantially over the area, with the maximum ellipticity reaching 8% (Figure 10b); higher ellipticities are observed in the the northwest and south-east corners of the survey area. In the deepest layer above the basement, the NMO ellipses are oriented close to the south-north direction, with the ellipticity somewhat increasing toward the south (Figure 10c).

The generalized Dix differentiation, as its conventional counterpart, suffers from amplification of errors for layers that are thin compared to their depth. The average relative thickness of the intervals used in our analysis reaches about 15%,

which is close to the limit of applicability of the Dix differentiation. The effective NMO velocities, however, were obtained by two sequential averaging procedures, which should have increased the stability of the interval moveout estimation. Indeed, the effective NMO ellipse was built by a 3-D semblance search for the whole superbin (which amounts to azimuthal averaging of NMO velocity) followed by the spatial smoothing of the NMO ellipses over the survey area. As discussed below, the results of our interval moveout analysis (Figure 10) are supported by independent borehole measurements and shear-wave data.

DISCUSSION AND CONCLUSIONS

We have developed and applied to field data a method of interval moveout analysis capable of separating the influence of azimuthal anisotropy and weak lateral velocity variation on normal-moveout velocity. The correction for lateral velocity variation in horizontally layered media depends on the shape (curvature) of the vertical-traveltime surface at the CMP location. Hence, obtaining the NMO ellipse for a reference laterally homogeneous medium does not require any information in addition to surface seismic data.

Our processing methodology consists of the following main steps:

1) **Azimuthal velocity analysis.**—We compute 3-D semblance as a function of vertical time at a fixed CMP location for all available data (i.e., including all source-receiver offsets and
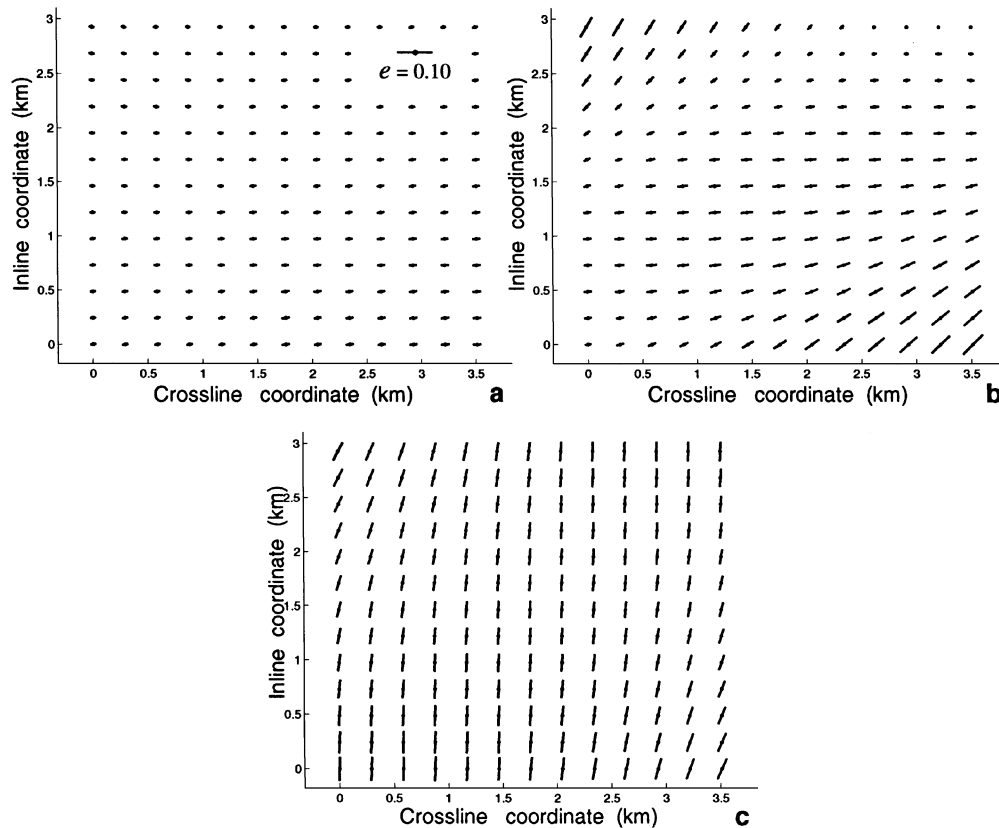

FIG. 10. Interval NMO ellipticities for the horizons between 1.5 and 1.84 s (a), 1.84 and 2.14 s (b), 2.14 and 2.57 s (c).

azimuths) using the hyperbolic moveout equation (1) parameterized by the NMO-velocity ellipse. As in the conventional velocity analysis, the semblance maximum at a certain vertical time indicates a reflection event. Azimuthal velocity analysis is not a model-dependent procedure and can be applied to any pure-mode reflection data.

2) Smoothing of the vertical traveltimes and effective NMO ellipses.—Smoothing is needed to reduce picking errors and compute vertical-traveltime surfaces and effective NMO ellipses suitable for the subsequent processing steps. Without careful smoothing we would not have been able to account for the lateral velocity variation in our case study and obtain meaningful interval NMO ellipses.

3) Correction for lateral heterogeneity.—The presence of lateral velocity variation significantly complicates the recovery of the interval moveout parameters from surface reflection data. Generally, moveout inversion in laterally heterogeneous anisotropic media would require tomographic algorithms based on anisotropic ray tracing. Here, we found a simple approximate way of correcting for *weak* lateral velocity variation in horizontally layered anisotropic models without ray tracing. However, we had to assume that not only the lateral variation in the elastic constants, but also the anisotropy is weak to be able to apply our equations to vertically inhomogeneous media. Our approximate solutions [equations (12) and (13)] indicate that the influence of lateral velocity variation on the NMO ellipses is controlled by the curvatuve of the vertical-traveltime surface $\tau(\mathbf{y})$, where $\mathbf{y}$ are the lateral (CMP) coordinates. Stable estimation of the curvature is impossible without smoothing the traveltime surface.

4) Generalized Dix differentiation.—After correcting the effective NMO ellipses for lateral velocity variation, one can obtain the *interval* NMO velocity by the generalized Dix differentiation (9). For most common azimuthally anisotropic models caused by a single system of vertical fractures, the semi-major axis of the P-wave interval NMO ellipse coincides with the fracture direction, while the fracture density is related to the difference between the semi-axes.

Applying this processing sequence to a "wide-azimuth" 3-D data set from the Powder River Basin, Wyoming, we obtained the interval P-wave NMO ellipses shown in Figure 10. Undoubtedly, the final result is influenced to a certain extent by a number of assumptions and approximations discussed above. Also, effective ellipticities are relatively small, which made the recovery of the anisotropic signature in moveout velocity rather difficult; we expect our methodology to be more robust in areas with a higher magnitude of azimuthal anisotropy and more substantial azimuthal variation of moveout velocity. Therefore, it is important to compare our conclusions with information about the fracture orientation obtained by other methods (D. Corrigan, personal communication):

1) The shallow section has fractures oriented approximately N110E. This is supported by outcrop measurements, FMI/FMS borehole scans and is recognizable on the rotational analysis of four-component S-wave data. The N110E orientation is in general agreement with our results for the layer immediately above $t = 1.84$ s.

2) Outcrop studies and analysis of a nine-component vertical seismic profiling (VSP) survey indicate that the fractures in the interval between $t = 1.84$ and 2.14 s are oriented approximately N70E. The same orientation was obtained by a layer-stripping analysis of the surface S-wave data. These are producing fractures whose orientation and density are of most interest from an exploration standpoint. The average azimuth of the semi-major axis of the NMO ellipse (Figure 10b) is indeed between N50E and N70E; note, however, that moveout data reveal substantial variability in both the direction and density of fractures.

3) Fracture orientation in the interval between $t = 2.14$ and 2.57 s is not as well established. However, there is some outcrop evidence for a south-north direction, which is close to the predominant orientation of the semi-major axis of the NMO ellipse.

One of the most important issues related to this analysis is which anisotropic coefficients can be estimated from the interval P-wave NMO ellipses. The answer is model-dependent and becomes increasingly complex for lower anisotropic symmetries. For the simplest azimuthally anisotropic model, horizontal transverse isotropy, the semi-major axis of the NMO ellipse is equal to the vertical P-wave velocity and points in the fracture direction (see the ticks in Figure 10). The difference between the semi-axes is roughly proportional to the anisotropic coefficient $\delta^{(V)}$, which is typically negative and depends on both the density and content of the cracks (Rüger, 1997; Tsvankin, 1997a). If the cracks are thin and filled with fluid, $\delta^{(V)}$ for formations with no equant porosity usually is close by absolute value to the fracture density (Tsvankin, 1997a). For dry cracks, however, $(-\delta^{(V)})$ may be about twice as large as the crack density, which shows the potential of P-wave data in evaluating the content of the cracks (Rüger and Tsvankin, 1997). On the other hand, spatial variations in the ellipticity may be caused, for instance, by the replacement of gas in the cracks with brine (or vice versa), rather than changes in the crack density. To estimate $\delta^{(V)}$ and the crack density separately, P-wave NMO velocity for horizontal events has to be combined with other data, such as the azimuthal AVO response (Rüger and Tsvankin, 1997), NMO velocity for dipping events (Contreras et al., 1999), time delays between split S-waves at vertical incidence or azimuthally dependent NMO velocity of the slow (SV) shear wave (Tsvankin, 1997a).

If the model is orthorhombic with a horizontal symmetry plane, the ellipticity is determined by the difference between the two anisotropic coefficients, $\delta^{(1)}$ and $\delta^{(2)}$, defined in the vertical symmetry planes of the medium (Tsvankin, 1997b). For orthorhombic media with a single fracture system, this difference is related to the crack density (it goes to zero if there are no fractures), and one of the semi-axes is parallel to the crack orientation. However, orthorhombic symmetry can also be caused by two orthogonal fracture systems, or two nonorthogonal systems with equal crack density. For these more complicated physical models the interpretation of the NMO ellipse becomes more ambiguous. Therefore, it is even more important to supplement P-wave moveout with additional data listed above.

It should be mentioned that for both HTI and orthorhombic media the axes of the P-wave NMO ellipse are parallel to the polarization vectors of two split shear waves at vertical incidence. More complex fracture models may have monoclinic symmetry (e.g., because of two unequal nonorthogonal sets of

cracks), for which the orientation of *P*-wave NMO ellipse deviates from the polarization directions of vertically traveling *S*-waves.

ACKNOWLEDGMENTS

We are grateful to Dennis Corrigan and Robert Withers of ARCO for providing the field data and sharing their knowledge of the processing and interpretation issues. We would also like to thank Bruce Mattocks, Bob Benson, and John Stockwell (all of CSM) for helping us with data processing. Support for this work was provided by the members of the Consortium Project on Seismic Inverse Methods for Complex Structures at the Center for Wave Phenomena, Colorado School of Mines and by the United States Department of Energy. I. Tsvankin was also supported by the Shell Faculty Career Initiation Grant.

REFERENCES

Alkhalifah, T., and Tsvankin, I., 1995, Velocity analysis in transversely isotropic media: Geophysics, **60**, 1550–1566.
Contreras, P., Grechka, V., and Tsvankin, I., 1999, Moveout inversion of *P*-wave data for horizontal transverse isotropy: Geophysics, **64**, 1219–1229.
Corrigan, D., Withers, R., Darnall, J., and Skopinski, T., 1996, Fracture mapping from azimuthal velocity analysis using 3-D surface seismic data: 66th Ann. Internat. Mtg., Soc. Expl. Geophys., Expanded Abstracts, 1834–1837.
Dix, C. H., 1955, Seismic velocities from surface measurements: Geophysics, **20**, 68–86.
Grechka, V., 1998, Transverse isotropy versus lateral heterogeneity in the inversion of *P*-wave reflection traveltimes: Geophysics, **63**, 204–212.
Grechka, V., and Cohen, J. K., 1996, Transverse isotropy versus lateral heterogeneity in inversion of *P*-wave reflection traveltimes: 66th Ann. Internat. Mtg., Soc. Expl. Geophys., Expanded Abstracts, 1503–1506.
Grechka, V., and McMechan, G. A., 1997, Analysis of reflection traveltimes in 3-D transversely-isotropic heterogeneous media: Geophysics, **62**, 1884–1895.
Grechka, V., and Tsvankin, I., 1998, 3-D description of normal moveout in anisotropic inhomogeneous media: Geophysics, **63**, 1079–1092.
Grechka, V., and Tsvankin, I., 1999, 3-D moveout velocity analysis and parameter estimation for orthorhombic media: Geophysics, **64**, 820–837.
Hubral, P., and Krey, T., 1980, Interval velocities from seismic reflection measurements: Soc. Expl. Geophys.
Lynn, H., Simon, K., Bates, C., and Van Doc, R., 1996, Azimuthal anisotropy in *P*-wave 3-D (multiazimuth) data: The Leading Edge, **15**, 923–928.
Press, W. H., Flannery, B. P., Teukolsky, S. A., and Vetterling, W. T., 1987, Numerical Recipes: The Art of Scientific Computing: Cambridge Univ. Press.
Rüger, A., 1997, *P*-wave reflection coefficients for transversely isotropic models with vertical and horizontal axis of symmetry: Geophysics, **62**, 713–722.
Rüger, A., and Tsvankin, I., 1997, Using AVO for fracture detection: Analytic basis and practical solutions: The Leading Edge, **16**, 1429–1434.
Thomsen, L., 1986, Weak elastic anisotropy: Geophysics, **51**, 1954–1966.
Tsvankin, I., 1997a, Reflection moveout and parameter estimation for horizontal transverse isotropy: Geophysics, **62**, 614–629.
——— 1997b, Anisotropic parameters and *P*-wave velocity for orthorhombic media: Geophysics, **62**, 1292–1309.
Tsvankin, I., Grechka, V., and Cohen, J. K., 1997, Generalized Dix equation and modeling of normal moveout in inhomogeneous anisotropic media: 67th Ann. Internat. Mtg., Soc. Expl. Geophys., Expanded Abstracts, 1246–1249.
Withers, R., and Corrigan, D., 1997, Fracture detection using wide azimuth 3-D seismic surveys: 59th EAGE Conference, Geneva, Extended Abstracts, Paper E003.

APPENDIX A

NMO ELLIPSE IN A LAYER WITH WEAK LATERAL VELOCITY VARIATION

Here, we obtain a first-order correction for the influence of weak lateral velocity variation (for brevity, we will call it lateral heterogeneity, or LH) on the NMO ellipse in a single horizontal anisotropic layer. The general 3-D NMO equation (2) parameterized by the matrix **W** [equation (3)] accounts for both anisotropy and lateral heterogeneity, unless deviations from hyperbolic moveout make the very notion of normal-moveout velocity meaningless. Our goal is to find the relationship between the matrix $\mathbf{W}^{\text{het}}$, responsible for the NMO ellipse in a LH layer, and the matrix $\mathbf{W}^{\text{hom}}$ for a reference homogeneous medium.

Assuming that lateral velocity variation is weak and following the approach developed by Grechka (1998) for vertical transverse isotropy, we apply first-order perturbation theory to express the matrix $\mathbf{W}^{\text{het}}$ as the sum of $\mathbf{W}^{\text{hom}}$ and small quantities related to LH. We restrict ourselves to anisotropic models with a horizontal symmetry plane (i.e., the medium can be transversely isotropic, orthorhombic, or monoclinic), which imposes additional constraints on the character of lateral velocity variation. While each elastic constant can vary laterally in a different fashion, it is assumed that these spatial variations do not destroy the symmetry of the phase- and group-velocity surfaces with respect to the horizontal plane.

Using equation (3) for a common midpoint (CMP) located at $\mathbf{y}\{y_1, y_2\} = 0$ (Figure A-1), we can write
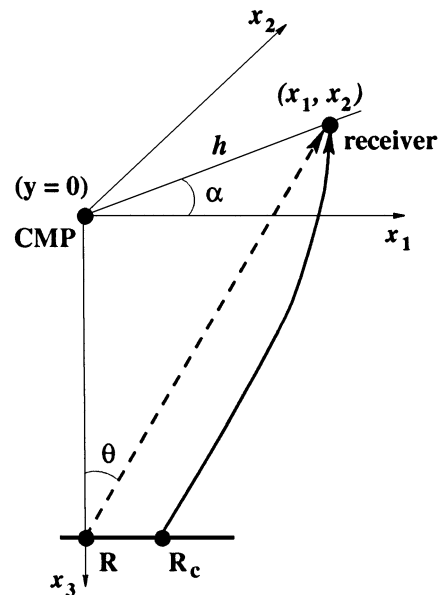

FIG. A.1. In the derivation of NMO velocity for a layer with a weak lateral velocity variation, the actual reflection raypath (solid) in CMP geometry can be replaced with a *non-specular* raypath (dashed) going through the zero-offset reflection point *R* in the *laterally homogeneous* layer.

$$W_{ij}^{\text{het}} = \tau_0^{\text{het}} \frac{\partial^2 \tau^{\text{het}}}{\partial x_i \partial x_j}\bigg|_{\mathbf{x}=0}, \qquad (i, j = 1, 2) \quad \text{(A-1)}$$

and

$$W_{ij}^{\text{hom}} = \tau_0^{\text{hom}} \frac{\partial^2 \tau^{\text{hom}}}{\partial x_i \partial x_j}\bigg|_{\mathbf{x}=0}, \qquad (i, j = 1, 2), \quad \text{(A-2)}$$

where τ^{het} and τ^{hom} are the one-way traveltimes from the zero-offset reflection point to the location $\mathbf{x}$ at the surface; $\tau_0^{\text{het}} = \tau^{\text{het}}(\mathbf{x}=0)$ and $\tau_0^{\text{hom}} = \tau^{\text{hom}}(\mathbf{x}=0)$ are the zero-offset traveltimes. τ^{hom} is obtained for a reference homogeneous layer with the parameters taken at the CMP. One-way traveltimes from the zero-offset reflection point appear in equations (A-1) and (A-2) because reflection-point dispersal has no influence on normal-moveout velocity, even if the medium is anisotropic and heterogeneous (Hubral and Krey, 1980; Grechka and Tsvankin, 1998).

Since the layer is horizontal and has a horizontal symmetry plane, in the absence of lateral heterogeneity the zero-offset reflection point R coincides with the projection of the CMP onto the boundary and has the coordinates $\{0, 0, x_3\}$ (Figure A 1). The traveltime τ^{hom} in the homogeneous layer is given by

$$\tau^{\text{hom}}(x_1, x_2) = \tau^{\text{hom}}(h, \alpha) = \frac{\sqrt{h^2 + x_3^2}}{g(\alpha, \theta)}, \qquad \text{(A-3)}$$

where x_1, x_2 are the receiver coordinates, $h = \sqrt{x_1^2 + x_2^2}$ is half the source-receiver offset, and $g(\alpha, \theta)$ is the group velocity as a function of the azimuth of the CMP line $\alpha = \tan^{-1}(x_2/x_1)$ and the polar angle $\theta = \tan^{-1}(h/x_3)$.

In general, lateral velocity variation leads to a shift of the zero-offset reflection point from R to a new location R_c (Figure A-1). Nonetheless, since LH is assumed to be weak (i.e., the quadratic and higher-order terms in the spatial derivatives of the elastic constants can be ignored), the traveltime perturbations that result from lateral velocity variation can be computed along the *unperturbed* ray propagating in the homogeneous model (Grechka and McMechan, 1997). Hence, we obtain the traveltime τ^{het} as an integral along the nonspecular raypath originated at point R to get

$$\tau^{\text{het}}(x_1, x_2) = \int_0^{\sqrt{h^2+x_3^2}} \frac{d\zeta}{g(\alpha, \theta, \zeta)}, \qquad \text{(A-4)}$$

where the group velocity g now depends on the distance ζ along the ray. Introducing the horizontal displacement along the ray (ξ), the traveltime can be rewritten as

$$\tau^{\text{het}}(x_1, x_2) = \frac{\sqrt{h^2 + x_3^2}}{h} \int_0^h \frac{d\xi}{g(\alpha, \theta, y_1(\xi), y_2(\xi))}; \qquad \text{(A-5)}$$

$$y_1 = \xi \cos\alpha \quad \text{and} \quad y_2 = \xi \sin\alpha. \qquad \text{(A-6)}$$

Assuming that the lateral variation in group velocity is sufficiently smooth, it can be expanded in a double Taylor series in the vicinity of the common midpoint $y_1 = y_2 = 0$:

$$g(\alpha, \theta, \xi) = g(\alpha, \theta, y_1, y_2)$$
$$= g_0 \left[1 + \frac{1}{g_0} \sum_{i=1}^{2} g_{,i} y_i + \frac{1}{g_0} \sum_{i,j=1}^{2} g_{,ij} y_i y_j + \cdots \right], \qquad \text{(A-7)}$$

where

$$g_0 \equiv g(\alpha, \theta, 0, 0), \qquad \text{(A-8)}$$

$$g_{,i} \equiv \frac{\partial g(\alpha, \theta, y_1, y_2)}{\partial y_i}\bigg|_{y_1=y_2=0}, \qquad \text{(A-9)}$$

and

$$g_{,ij} \equiv \frac{\partial^2 g(\alpha, \theta, y_1, y_2)}{\partial y_i \partial y_j}\bigg|_{y_1=y_2=0}. \qquad \text{(A-10)}$$

Since the lateral velocity variation is weak, all terms involving y_i in equation (A-7) are small compared to unity, and in the linear approximation

$$\frac{1}{g(\alpha, \theta, y_1, y_2)}$$
$$= \frac{1}{g_0} \left[1 - \frac{1}{g_0} \sum_{i=1}^{2} g_{,i} y_i - \frac{1}{g_0} \sum_{i,j=1}^{2} g_{,ij} y_i y_j - \cdots \right]. \qquad \text{(A-11)}$$

Substituting equations (A-6), (A-8)–(A-11) into (A-5) and evaluating the integral yields

$$\tau^{\text{het}}(x_1, x_2) = \frac{\sqrt{h^2 + x_3^2}}{g_0} \bigg[1 - \frac{h}{2g_0} (g_{,1} \cos\alpha + g_{,2} \sin\alpha)$$
$$- \frac{h^2}{6g_0} (g_{,11} \cos^2\alpha + 2g_{,12} \sin\alpha \cos\alpha$$
$$+ g_{,22} \sin^2\alpha) - \cdots \bigg]. \qquad \text{(A-12)}$$

From equation (A-3) it is clear that the term in front of the brackets in equation (A-12) is the traveltime $\tau^{\text{hom}}(x_1, x_2)$. Using the relations $x_1 = h \cos\alpha$ and $x_2 = h \sin\alpha$ (Figure A-1), equation (A-12) can be rewritten in the form

$$\tau^{\text{het}}(x_1, x_2) = \tau^{\text{hom}}(x_1, x_2) \bigg[1 - \frac{1}{2g_0} (g_{,1}x_1 + g_{,2}x_2)$$
$$- \frac{1}{6g_0} (g_{,11}x_1^2 + 2g_{,12}x_1x_2 + g_{,22}x_2^2) - \cdots \bigg]. \qquad \text{(A-13)}$$

Equation (A-13) expresses the contribution of the lateral velocity variation to the one-way traveltime in terms of the spatial derivatives of the group-velocity function. Note that since we

ignored the influence of LH on reflection-point dispersal, the zero-offset ray in the LH layer remains vertical, and

$$\tau_0^{\text{het}} = \tau_0^{\text{hom}}. \qquad (\text{A-14})$$

To obtain the matrix $\mathbf{W}^{\text{het}}$ defined by equation (A-1), we need to find the second-order partial derivatives of the traveltime τ^{het} [equation (A-13)] with respect to the coordinates (x_1, x_2) at zero offset $\mathbf{x} = 0$:

$$\frac{\partial^2 \tau^{\text{het}}}{\partial x_i \partial x_j}\bigg|_{\mathbf{x}=0} = \frac{\partial^2 \tau^{\text{hom}}}{\partial x_i \partial x_j}\bigg|_{\mathbf{x}=0} - \frac{\partial \tau^{\text{hom}}}{\partial x_i}\bigg|_{\mathbf{x}=0} \frac{g_{,j}}{2g_0} - \frac{\partial \tau^{\text{hom}}}{\partial x_j}\bigg|_{\mathbf{x}=0}$$

$$\times \frac{g_{,i}}{2g_0} - \tau_0^{\text{hom}}\left[\frac{\partial}{\partial x_i}\left(\frac{g_{,j}}{2g_0}\right) + \frac{\partial}{\partial x_j}\left(\frac{g_{,i}}{2g_0}\right) + \frac{g_{,ij}}{3g_0}\right]\bigg|_{\mathbf{x}=0}. \qquad (\text{A-15})$$

The second and third terms on the right-hand side of equation (A-15) depend on the horizontal components of the slowness vector $\mathbf{p}$ in the homogeneous layer:

$$\frac{\partial \tau^{\text{hom}}}{\partial x_i} \equiv p_i. \qquad (\text{A-16})$$

At zero offset, $p_1|_{\mathbf{x}=0} = p_2|_{\mathbf{x}=0} = 0$ because the slowness vector of the zero-offset ray is vertical [it has to be orthogonal to the (horizontal) reflector], so the terms containing $(\partial\tau^{\text{hom}}/\partial x_i)$ and $(\partial\tau^{\text{hom}}/\partial x_j)$ go to zero.

Next, let us show that the terms $(\partial/\partial x_i)(g_{,j}/2g_0)$ and $(\partial/\partial x_j)(g_{,i}/2g_0)$ in equation (A-15) vanish as well. Indeed, g_0

is an even function of x_1 and x_2 because the group velocity in a medium with a horizontal symmetry plane is symmetric with respect to vertical in any vertical plane. The derivatives of group velocity with respect to y_i ($g_{,1}$ and $g_{,2}$) also have to be even functions of x_1 and x_2; otherwise, the symmetry of group velocity with respect to the horizontal plane will not be preserved away from the CMP location. Therefore, the derivatives of $(g_{,j}/2g_0)$ and $(g_{,i}/2g_0)$ with respect to x_1 and x_2 go to zero at $\mathbf{x} = 0$.

Thus, equation (A-15) reduces to

$$\frac{\partial^2 \tau^{\text{het}}}{\partial x_i \partial x_j}\bigg|_{\mathbf{x}=0} = \frac{\partial^2 \tau^{\text{hom}}}{\partial x_i \partial x_j}\bigg|_{\mathbf{x}=0} - \tau_0^{\text{hom}} \frac{g_{,ij}}{3g_0}\bigg|_{\mathbf{x}=0}. \qquad (\text{A-17})$$

The group velocity g_0 and its spatial derivatives $g_{,ij}$ in equation (A-17) are evaluated at the zero offset $\mathbf{x} = 0$, i.e., for the vertical ray emanating from the zero-offset reflection point. Since in a medium with a horizontal symmetry plane the vertical phase and group velocities are equal to each other, we can replace g_0 and $g_{,ij}$ with the vertical phase velocity V_0 and its derivatives with respect to y_i. Finally, multiplying equation (A-17) by $\tau_0^{\text{het}} = \tau_0^{\text{hom}} = \tau_0$ [see equation (A-14)], we obtain the following relationship between the matrices $\mathbf{W}^{\text{hom}}$ and $\mathbf{W}^{\text{het}}$:

$$W_{ij}^{\text{het}} = W_{ij}^{\text{hom}} - \frac{\tau_0^2}{3\,V_0}\frac{\partial^2 V_0}{\partial y_i \partial y_j}\bigg|_{\mathbf{y}=0}, \qquad (i, j = 1, 2). \qquad (\text{A-18})$$

Thus, in the linear approximation employed here, the influence of lateral velocity variation on the NMO ellipse is proportional to the *curvature* of the vertical-velocity surface $V_0(\mathbf{y})$ at the CMP location.

APPENDIX B

NMO ELLIPSE IN A TWO-LAYERED MODEL WITH WEAK LATERAL VELOCITY VARIATION

Here, we extend the derivation from Appendix A to a model that contains two horizontal anisotropic layers with lateral velocity variation. In addition to the assumptions used in Appendix A (the horizontal plane is a plane of symmetry, the lateral heterogeneity is weak), we will consider only *weakly anisotropic* media. The weak-anisotropy assumption makes it possible not only to simplify the derivation, but also to obtain the final expression for the NMO ellipse in terms of quantities that can be measured from reflection seismic data—the effective NMO velocities and zero-offset traveltimes for reflections from the two interfaces of our model (Figure B-1).

In the model without lateral velocity variation, the one-way traveltime τ^{hom} from the zero-offset reflection point to the surface is given by

$$\tau^{\text{hom}}(h) \equiv \tau_1^{\text{hom}} + \tau_2^{\text{hom}} = \frac{\sqrt{\left(h^{(1)}\right)^2 + \left(x_3^{(1)}\right)^2}}{g^{(1)}}$$

$$+ \frac{\sqrt{\left(h^{(2)}\right)^2 + \left(x_3^{(2)}\right)^2}}{g^{(2)}}, \qquad (\text{B-1})$$

where $g^{(1)}$ and $g^{(2)}$ are the group velocities along the ray (Figure B-1) and $h = h^{(1)} + h^{(2)}$ is half the source-receiver offset. For convenience, we denote
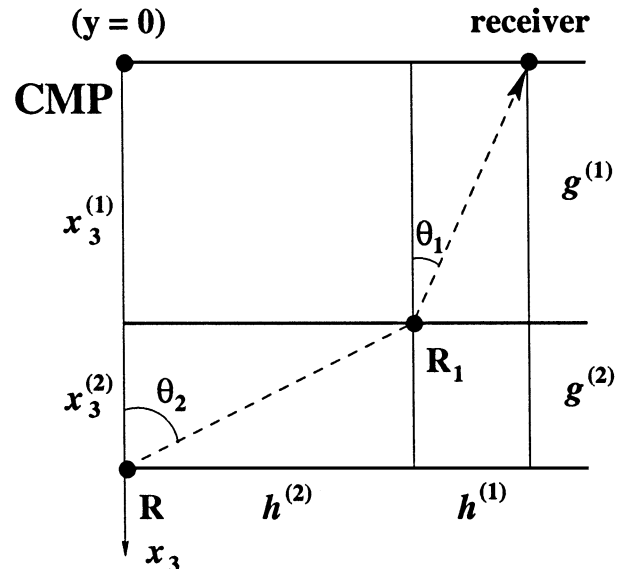

FIG. B.1. The projection of the nonspecular raypath from the zero-offset reflection point onto the vertical plane that contains the CMP line.

$$h^{(2)} = kh \quad \text{and} \quad h^{(1)} = (1-k)h. \quad (B\text{-}2)$$

Despite the presence of the horizontal symmetry plane in each layer, the influence of *depth-varying* azimuthal anisotropy forces the ray to deviate from the vertical incidence plane shown in Figure B-1. This deviation, however, produces traveltime distortions *quadratic* in the anisotropy coefficients (Grechka and Tsvankin, 1998) because the traveltime in the linearized weak-anisotropy approximation can always be calculated along the unperturbed ray. Here, we restrict ourselves to linear terms in the anisotropy coefficients and evaluate the traveltimes in both homogeneous and LH models along the rays confined to the vertical incidence plane.

The one-way traveltime τ^{het} in the model with lateral velocity variation can be found by analogy with equation (A-5):

$$\tau^{\text{het}}(h) = \frac{\sqrt{\left(h^{(1)}\right)^2 + \left(x_3^{(1)}\right)^2}}{h^{(1)}} \int_{h^{(2)}}^{h} \frac{d\xi}{g^{(1)}(\xi)}$$

$$+ \frac{\sqrt{\left(h^{(2)}\right)^2 + \left(x_3^{(2)}\right)^2}}{h^{(2)}} \int_0^{h^{(2)}} \frac{d\xi}{g^{(2)}(\xi)}, \quad (B\text{-}3)$$

where ξ is the horizontal displacement along the ray.

Expanding the interval group velocities $g^{(1)}$ and $g^{(2)}$ near the CMP in a double Taylor series in the horizontal coordinates [see equation (A-7)] and evaluating the integrals in equation (B-3), we express τ^{het} through the traveltimes τ_1^{hom} and τ_2^{hom} in the laterally homogeneous model as

$$\tau^{\text{het}}(\mathbf{x}) = \tau_1^{\text{hom}}(\mathbf{x}) \left[1 - \frac{1+k}{2\,g_0^{(1)}} \left(g_{,1}^{(1)} x_1 + g_{,2}^{(1)} x_2 \right) \right.$$

$$\left. - \frac{1+k+k^2}{6\,g_0^{(1)}} \left(g_{,11}^{(1)} x_1^2 + 2\,g_{,12}^{(1)} x_1 x_2 + g_{,22}^{(1)} x_2^2 \right) \right]$$

$$+ \tau_2^{\text{hom}}(\mathbf{x}) \left[1 - \frac{k}{2\,g_0^{(2)}} \left(g_{,1}^{(2)} x_1 + g_{,2}^{(2)} x_2 \right) \right.$$

$$\left. - \frac{k^2}{6\,g_0^{(2)}} \left(g_{,11}^{(2)} x_1^2 + 2\,g_{,12}^{(2)} x_1 x_2 + g_{,22}^{(2)} x_2^2 \right) \right],$$

$$(B\text{-}4)$$

where $x_1 = h\cos\alpha$, $x_2 = h\sin\alpha$ (α is the azimuth of the CMP line), and $g_0^{(1,2)}$, $g_{,i}^{(1,2)}$, and $g_{,ij}^{(1,2)}$ are defined in the same way as g_0, $g_{,i}$, and $g_{,ij}$ in Appendix A.

Next, we express the parameter k [equation (B-2)] in terms of the velocities and traveltimes. In the weak anisotropy limit, Snell's law at the transmission point R_1 (Figure B-1) can be written as

$$\frac{\sin\theta_1}{g^{(1)}} = \frac{\sin\theta_2}{g^{(2)}}, \quad (B\text{-}5)$$

where the *phase* velocities in both layers were replaced with the *group* velocities. Multiplying the numerator and denominator on both sides of equation (B-5) by the corresponding ray lengths in each layer $\ell^{(1,2)} = \tau_{1,2}^{\text{hom}} g^{(1,2)}$ yields (see Figure B-1)

$$\frac{h^{(1)}}{\tau_1^{\text{hom}} \left(g^{(1)}\right)^2} = \frac{h^{(2)}}{\tau_2^{\text{hom}} \left(g^{(2)}\right)^2}. \quad (B\text{-}6)$$

From equation (B-6) and the definition of k [equation (B-2)] it

follows that

$$k = \frac{\tau_2^{\text{hom}} \left(g^{(2)}\right)^2}{\tau_1^{\text{hom}} \left(g^{(1)}\right)^2 + \tau_2^{\text{hom}} \left(g^{(2)}\right)^2}. \quad (B\text{-}7)$$

Note that the dependence of k on $\mathbf{x}$ in equation (B-4) for small incidence angles can be neglected. Indeed, when replacing the sines with tangents in equation (B-5), we find

$$\frac{1-k}{k} = \frac{g^{(1)} x_3^{(1)}}{g^{(2)} x_3^{(2)}}. \quad (B\text{-}8)$$

Although the ratio of the group velocities $g^{(1)}/g^{(2)}$ (and k) does change with $\mathbf{x}$, the offset-dependent terms are entirely a result of the anisotropy and lateral velocity variation. Hence, these terms can be ignored in equation (B-4), where they are multiplied with small quantities related to lateral variation in group velocity.

To obtain the matrix $\mathbf{W}^{\text{het}}$, it is necessary to evaluate the second-order partial derivatives of equation (B-4) with respect to x_1 and x_2 at the CMP location ($\mathbf{x} = 0$). Since the interfaces are horizontal and the horizontal plane is a plane of symmetry, $\partial \tau_{1,2}^{\text{hom}}/\partial x_i$ and $\partial g^{(1,2)}/\partial x_i$ vanish at $\mathbf{x} = 0$ (see Appendix A). Taking this into account and ignoring the dependence of k on $\mathbf{x}$ (see above), we obtain

$$\left. \frac{\partial^2 \tau^{\text{het}}}{\partial x_i \partial x_j} \right|_{\mathbf{x}=0} = \left. \frac{\partial^2}{\partial x_i \partial x_j} \left(\tau_1^{\text{hom}} + \tau_2^{\text{hom}} \right) \right|_{\mathbf{x}=0}$$

$$- \left[\frac{1+k+k^2}{3\,g_0^{(1)}} \tau_1^{\text{hom}} g_{,ij}^{(1)} + \frac{k^2}{3\,g_0^{(2)}} \tau_1^{\text{hom}} g_{,ij}^{(2)} \right]_{\mathbf{x}=0}. \quad (B\text{-}9)$$

Multiplying equation (B-9) by the zero-offset traveltime

$$\tau_0 \equiv \tau_0^{\text{het}} = \tau_0^{\text{hom}} = \tau_{01}^{\text{hom}} + \tau_{02}^{\text{hom}} \equiv \tau_{01} + \tau_{02} \quad (B\text{-}10)$$

and using the definitions of the matrices $\mathbf{W}^{\text{het}}$ and $\mathbf{W}^{\text{hom}}$ [equations (A-1) and (A-2)] yields

$$W_{ij}^{\text{het}} = W_{ij}^{\text{hom}} - \frac{\tau_0}{3} \left[\frac{(1+k+k^2)\tau_{01}}{g_0^{(1)}} g_{,ij}^{(1)} \right.$$

$$\left. + \frac{k^2 \tau_{02}}{g_0^{(2)}} g_{,ij}^{(2)} \right]_{\mathbf{x}=0}, \quad (i,j = 1, 2).$$

$$(B\text{-}11)$$

Since both reflectors in our model are horizontal (see Figure B-1), the second-order partial derivatives of the vertical velocities $g_{,ij}^{(1)}$ and $g_{,ij}^{(2)}$ in equation (B-11) can be experessed in terms of derivatives of the vertical traveltimes. Differentiating equations $\tau_{0\ell} g_0^{(\ell)} = \text{const}$, $(\ell = 1, 2)$ twice with respect to spatial coordinates y_i gives in the linear approximation [see equation (11)]

$$\tau_{0\ell} g_{,ij}^{(\ell)} = -\tau_{0\ell,ij} g_0^{(\ell)}, \quad (B\text{-}12)$$

where $\tau_{0\ell,ij} \equiv \partial^2 \tau_{0\ell}/\partial y_i \partial y_j$. Substituting equations (B-12) into equations (B-11) yields

$$W_{ij}^{\text{het}} = W_{ij}^{\text{hom}} + \frac{\tau_0}{3} \left[(1+k+k^2)\tau_{01,ij} + k^2 \tau_{02,ij} \right],$$

$$(i,j = 1, 2). \quad (B\text{-}13)$$

The derivative $\tau_{02,ij}$ can be expressed in terms of τ_0 and τ_{01} using equation (B-10) to yield

$$\tau_{02,ij} = \tau_{0,ij} - \tau_{01,ij}, \qquad (i,j = 1,2). \quad \text{(B-14)}$$

Substituting equation (B-14) into (B-13), we find the matrix $\mathbf{W}^{\text{het}}$ as

$$W_{ij}^{\text{het}} = W_{ij}^{\text{hom}} + \frac{\tau_0}{3}\left[k^2\tau_{0,ij} + (1+k)\tau_{01,ij}\right],$$
$$(i,j = 1,2). \quad \text{(B-15)}$$

The value of k at zero offset is given by equation (B-7) with the vertical group velocities and traveltimes. In the weak anisotropy approximation, the vertical velocities $g_0^{(1,2)}$ can be replaced further with the interval normal-moveout velocities $V_{\text{cir}}^{(1,2)}$ [equation (15)] because $g_0^{(1,2)}$ contribute only to the already small terms that involve lateral velocity variation. Then equation (B-7) becomes

$$k = \frac{\tau_{02}\left(V_{\text{cir}}^{(2)}\right)^2}{\tau_{01}\left(V_{\text{cir}}^{(1)}\right)^2 + \tau_{02}\left(V_{\text{cir}}^{(2)}\right)^2}. \quad \text{(B-16)}$$

The interval NMO velocity in the second layer $V_{\text{cir}}^{(2)}$ cannot be obtained directly from reflection data. To express $V_{\text{cir}}^{(2)}$ through the effective NMO velocities for reflections from the bottom of the first ($V_{\text{cir}}^{(1)}$) and second (V_{cir}) layer, we use the conventional Dix (1955) formula:

$$\tau_0 V_{\text{cir}}^2 = \tau_{01}\left(V_{\text{cir}}^{(1)}\right)^2 + \tau_{02}\left(V_{\text{cir}}^{(2)}\right)^2. \quad \text{(B-17)}$$

In general, normal-moveout velocity in azimuthally anisotropic media should be obtained by averaging the interval NMO *ellipses* rather than the NMO velocities at a particular azimuth (Tsvankin et al., 1997). Nonetheless, Tsvankin et al. (1997) also show that the conventional Dix equation (B-17) provides a linear approximation (in the anisotropic coefficients) to the exact "generalized" Dix-type averaging of the NMO ellipses.

Substituting equation (B-17) into equation (B-16) and using relation (B-10) allows us to express k in terms of quantities that can be obtained from reflection data:

$$k = 1 - \frac{\tau_{01}\left(V_{\text{cir}}^{(1)}\right)^2}{\tau_0 V_{\text{cir}}^2}. \quad \text{(B-18)}$$

Hence, the final result is given by equation (B-15) with k defined in equation (B-18).